



Titanium Dioxide (TiO₂) Sensitized Zinc Oxide (ZnO)/Conducting Polymer Nanocomposites for Improving Performance of Hybrid Flexible Solar Cells

Surbhi Pathania² · Jehova Jire L. Hmar¹ · Bandhna Verma² · Tanmoy Majumder³ · Vinay Kumar² · P. Chinnamuthu⁴

Received: 6 March 2022 / Accepted: 1 July 2022 / Published online: 20 July 2022
© The Minerals, Metals & Materials Society 2022

Abstract

This paper focuses on improvement of power conversion efficiency (PCE) of flexible solar cell based on ZnO-TiO₂/PVK/PEDOT:PSS heterostructures. ZnO nanorods and ZnO-TiO₂ nanosheets have been synthesized by a hydrothermal method and layer-by-layer adsorption and reaction (LBLAR), respectively. The structural, optical and morphological properties are investigated using XRD spectroscopy, UV-Vis spectroscopy and field emission scanning electron microscopy, respectively. The TiO₂/ZnO nanosheets provide increased interfacial area for charge separation of the active area, as well as a dense network of pathways for improved charge transport. We have fabricated PET/ITO/ZnO-TiO₂/PVK/PEDOT:PSS/Ag (denoted as D1), PET/ITO/ZnO/PVK/PEDOT:PSS/Ag (denoted as D2) and PET/ITO/PVK/PEDOT:PSS/Ag (denoted as D3) solar cell devices on flexible PET substrate. The flexible D1 device shows better PCE value up to 2.76% as compared to control devices D2 and D3 due to the presence of an electron transport layer of TiO₂ and hole transport conducting polymer layer of PVK that forms an effective interface for enhancing of electron–hole pair generation and better charge separation. The PCE value of the flexible D1 device remained unchanged even after bending the device at 80°, 90°, 110°, 150° bending angles, which demonstrates that the fabricated D1 device is suitable for flexible solar cell applications.

✉ Jehova Jire L. Hmar
jehovajire52@gmail.com; jehova@nsut.ac.in

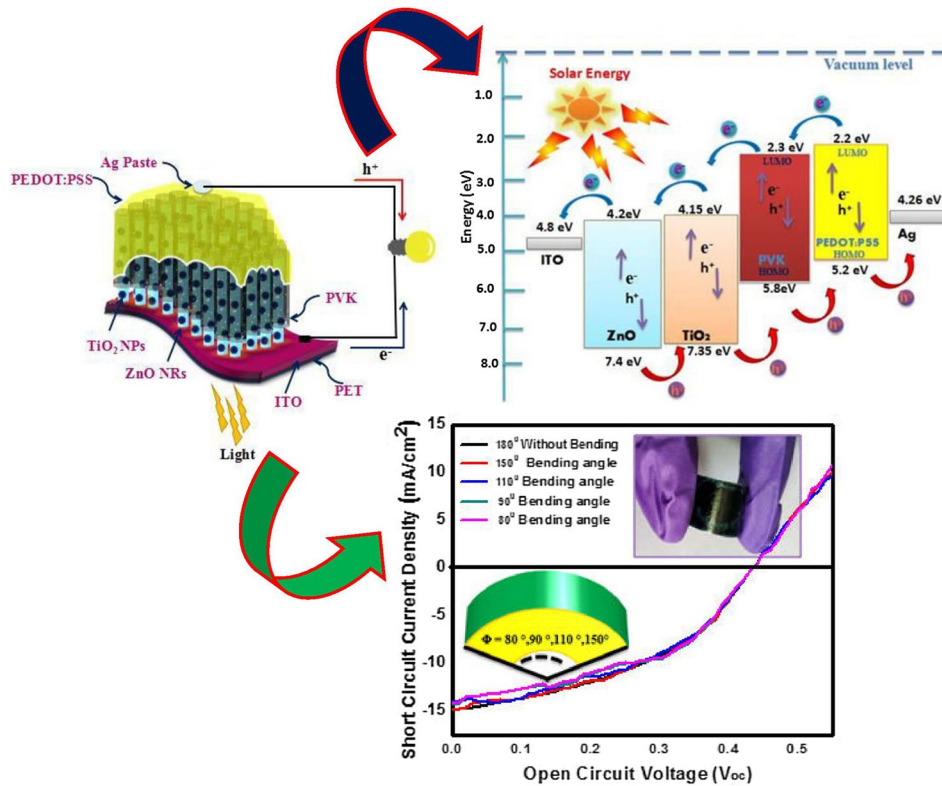
¹ Department of Physics, Netaji Subhas University of Technology (NSUT), Sector-3, Dwarka, New Delhi 110078, India

² Department of Physics and Astronomical Sciences, Central University of Jammu, Rahya-Suchani, Samba, J&K 181143, India

³ Department of Electronics and Communication Engineering, Tripura Institute of Technology Agartala, Agartala 799015, India

⁴ Department of ECE, NIT Nagaland, Dimapur 797103, India

Graphical Abstract



Keywords TiO₂/ZnO nanosheets · ITO/ZnO-TiO₂/PVK/PEDOT:PSS device · power conversion efficiency · hybrid flexible solar cell

Introduction

The generation of electricity from solar energy conversion by photovoltaic devices has gained a lot of interest as the demand for clean and renewable energy is increasing.¹ Hybrid solar cells are of growing interest because of diverse benefits and the advantage of a combination of both organic and inorganic semiconductors. The two semiconductors, of inorganic and organic material, are assembled together in a heterojunction-type photoactive layer, which can have greater power conversion efficiency (PCE) than a single material. Organic materials that consist of conjugated polymers act as the photon absorber and exciton donor. The lower electron mobility than hole mobility in these conjugated polymers result in lower device efficiency.² The hybrid inorganic–organic solar cell devices use the property of high carrier mobility in inorganic semiconductors to curb charge transport limitations of the organic phase. The inorganic material facilitates exciton dissociation at the junction. Charge is transferred and then separated after an exciton created in the donor is delocalized on a donor–acceptor complex.

However, the device morphology is a key factor to improve the efficiency of hybrid solar cells. The proper intermixing of the polymer and nanocrystals creates efficient charge separation, but it is not good for the charge transport to the electrodes. Therefore, to make a hybrid photovoltaic device with improved power conversion efficiency, a compromise solution is needed for charge separation as well as charge transport. There have been numerous reports on efficient charge separation using metal-oxide semiconductors/organic polymer composites.^{3–8} The inorganic metal oxide and polymer-based solar devices can be designed in two ways. One is blending of metal-oxide and polymer together to form heterojunction device. Other method is infiltration of polymers over metal oxide-based nanostructures grown on the flexible substrates. The latter method provides the advantage of well-connected transport paths in metal oxide semiconductors.⁹ The inorganic metal oxide semiconductor as an electron transport layer plays a dramatic role in charge separation and charge transport eradicating the electrical shunts between transparent electrode and hole transport material interfaces. Inorganic metal oxide semiconductors such as TiO₂, ZnO, and SnO₂ are

commonly used as electron transport layers with great stability and brilliant electronic properties.^{10–14} Zinc oxide (ZnO) is of interest because of its *n*-type conductivity,¹⁵ high band gap, high electron mobility, nontoxicity and environmentally friendly properties. ZnO nanostructures have found widespread application in ultraviolet lasers, light emitting diodes, detectors and photovoltaic cells.^{16–20} ZnO nanorods grown perpendicular to the substrate are particularly interesting. This has both the advantages of increasing the donor–acceptor interfacial area and creating electron transport pathways toward the electrode that possess very high electron mobility. Vertically aligned ZnO nanorods depend upon the quality of the interface between organic and inorganic nanostructures.²¹ Tian et al. designed ZnO based on assembled nanorods and nanosheets for photovoltaic devices. The nanorod diameters and spacing between them can be regulated to generate a structure with a large interfacial contact area yet permitting adequate polymer filling of the gaps.^{22,23} TiO₂ decorated on ZnO nanostructures can improve the photoabsorption and photocurrent generation of the proposed hybrid photovoltaic device. Kim et al. demonstrated the use of a TiO₂ interfacial layer between the active layer and an Al electrode which resulted in reduction of carrier recombination and also increased the value of Voc.²⁴ TiO₂ nanostructures are attractive due to their nontoxic nature and excellent size tunability. Hannachi and others also reported that 1-D TiO₂ nanostructures help in filling the pores between existing YBCO grains.²⁵ However, in photovoltaic devices, TiO₂ commonly acts as the electron transport layer as well as optical spacer.²⁶ Wu et al. reported that quantum yield for electron injection from polymer to oxide array is higher in TiO₂-based hybrid solar cells than ZnO-based hybrid solar cells.²⁷ The TiO₂/ZnO bilayer possesses the advantages of high electron extraction and reduction of interfacial recombination. The photoactive layer in hybrid solar cells plays an important role in effective charge extraction towards the electrodes restricting any loss such as charge recombination and exciton quenching at the interfaces.²⁸ Rani et al. demonstrated TiO₂/ZnO composite-based solar cells improved photovoltaic properties as compared to either TiO₂ or ZnO solar cells.²⁹ Because of their versatile chemical structure, high mechanical flexibility and low-cost fabrication, conjugated polymers have been used as the photoactive component in solar cells, photodiodes and memory devices. The photoexcitation of organic polymers results in exciton generation which are separated at the interface between *p*-type (electron-donating) and *n*-type (electron-accepting) material. The blending of electron acceptors into polymers may effect their hole mobility.³⁰ In order to increase the interfacial area between *p*-type and *n*-type materials, a conjugated polymer infiltrating a nanoporous

semiconductor is an appealing choice.³¹ PVK has become one of the best photoconductive polymers for electronic and optical applications because of its effective hole-transport ability. PVK is a *p*-type organic polymer with absorption in the UV region. Wang et al. demonstrated a hybrid UV photodetector by using ZnO nanorods and PVK as the electron acceptor and donor, respectively.^{32–35} When the ZnO NRs are embedded in polymers such as PVK, photogenerated excitons can be efficiently separated to the adjacent layer as exciton binding energy is reduced.³⁶ PEDOT:PSS thin film is highly transparent in the visible light range. PEDOT:PSS possesses high mechanical flexibility, excellent thermal stability and low cost. The work function of PEDOT:PSS film is 5.0 to 5.2 eV which makes it favourable for charge injection and charge transfer.^{37–40} Thu et al. revealed that intrinsic charges in the metal oxide restrict photocurrent generation, and a low metal oxide work function is favourable for a large driving force for exciton separation.⁴¹

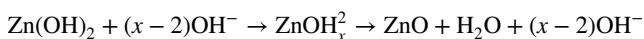
In this present study, we propose to undertake a systematic study for the use of aligned ZnO nanorods and nanocrystals for TiO₂ hybrid photovoltaic devices which are low cost, nontoxic and environmentally friendly. In this report, we have synthesized ZnO nanorods on flexible polymer PET (polyethylene terephthalate) substrates using a hydrothermal method. We have also attached TiO₂ nanoparticles on ZnO nanorods using layer-by-layer adsorption and reaction (LBLAR). It is observed that after attaching of TiO₂ on ZnO nanorods, nanosheet structures were obtained which are quite interesting for photovoltaic performance due to highly dense pathways available for charge transport. The inverted device design has been shown to better harvest incoming light due to a more favourable electromagnetic field distribution inside the active layer. By inverting the charge collection process, i.e. collection of holes via the top electrode and electrons via the back electrode, an efficient charge separation process can be achieved. Our motivation is to design a typical inverted flexible solar cell device structure for effective charge separation and fast charge transport. We have fabricated a solar cell where the ITO electrode acts as a cathode, ZnO and TiO₂ act as electron transport layers, PVK and PEDOT:PSS are selected as hole transport layers and the semi-transparent Ag electrode acts as anode. Ag as the top metal electrode is a good choice because of its intrinsic stability in air, hole extraction capability and better matching with the hole transporting polymer layer. The photoactive layer is TiO₂-PVK where PVK acts as charge receptor material and the generated excitons in PVK move towards the large interface between PVK and TiO₂ for charge separation. The free electrons then move to the conduction band of the TiO₂ and further drift to the cathode. TiO₂ is used to improve the interface states between ZnO and PVK. The shape and size of the resultant nanostructure

arrays have been studied through field emission scanning electron microscopy (FESEM). The optical characteristics of ZnO nanorods and ZnO/TiO₂ nanosheets have been studied through UV-Vis spectroscopy, FTIR spectroscopy and Raman spectroscopy. The J-V characteristics of the device were measured using Solar Simulator.

Experimental

Hydrothermal Synthesis of ZnO Nanorods

For the growth of ZnO nanorods, a hydrothermal method was used which has been reported in earlier literature.^{42–44} To grow ZnO nanorods, flexible ITO-coated PET was used as substrate. The PET substrate was cleaned using acetone and DI water. Using a spin coating method, a thin seed layer of ZnO nanoparticles was first deposited on cleaned ITO-coated flexible PET substrates. The ZnO nanoparticle seed layer solution was made using the sol-gel method, which involved dissolving 0.01 M zinc acetate (Merck, 99%) in 2-propanol (Merck, 99%) with continuous heating and stirring at 65°C on a magnetic stirrer. After 30 min, diethanolamine (Merck, 99%) was added to the previous solution drop-by-drop resulting in a transparent solution. The solution was allowed to cool for half an hour at room temperature. ZnO nanoparticle seed layers were then deposited on the ITO-coated flexible PET substrates with a spin speed of 2000 rpm for 80 s. ZnO thin films were annealed for 3 h at 100°C to remove the solvents. These seeded substrate films were vertically placed in borosil bottles containing an equimolar aqueous solution of zinc nitrate and hexamethylenetetramine (HMTA) as a precursor solution. The hydrothermal growth was done by placing sealed borosil bottles in an oil bath for 4 h at a reaction temperature of 90°C. In the following reactions, zinc nitrate produces Zn²⁺ ions and HMTA provides an alkaline environment that produces the OH⁻ ions. The growth process occurs due to a dissolution-secondary precipitation mechanism and the following reaction is:



As-prepared samples were then rinsed with distilled water and dried in air for further use.

Attachment of TiO₂ Using LBLAR

Layer-by-layer adsorption and reaction (LBLAR) was employed to deposit the TiO₂ coating layer on the surface of the ZnO nanorods represented in Fig. 1. The as-obtained ZnO nanorod array film was successively immersed into three different solutions for 40 s each, which were TiO₂ solution, pure ethanol and deionized water, respectively. Then

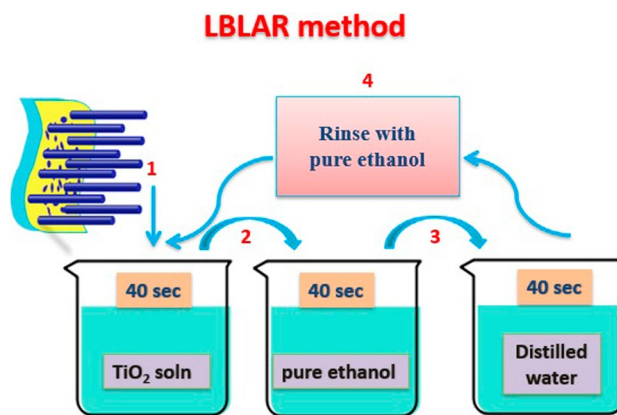
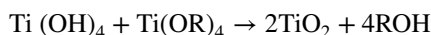
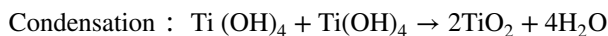
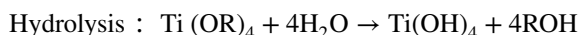


Fig. 1 Schematic diagram showing the synthesis process of TiO₂ by layer-by-layer adsorption and reaction (LBLAR).

the film was rinsed with pure ethanol to dissolve excess water and weakly bound TiO₂ before the next dipping. Different cycles were repeated according to the requirement of the thickness of TiO₂ coating layer.⁴⁵ In our case, we have applied five repetitive cycles. The TiO₂ solution was prepared by dissolving titanium butoxide (Ti(OBu)₄) and deionized water in a 1:20 molar ratio with heating and stirring at 65°C. After 15 min, HCl was added to prevent agglomeration of TiO₂ nanoparticles and it works as a stabilizing agent. The chemical reaction for hydrolysis and condensation is given by



where R is the component of a Ti (IV)-butoxide that designates a butyl-group with the general formula C₄H₉. Basically, optimum concentrations of acidity (OH⁻/H⁺ ratio) are crucial for crystal orientation. As-prepared TiO₂/ZnO films were calcined at 150°C for about 1 h.

Device Fabrication of the ITO/ZnO-TiO₂/PVK/PEDOT:PSS/Ag Heterojunction

A hybrid ITO/ZnO-TiO₂/PVK/PEDOT:PSS/Ag heterojunction photovoltaic device was fabricated by dip coating the prepared TiO₂/ZnO NRs films with ITO as the back electrode on flexible PET substrate in PVK solution. PVK solution was prepared by dissolving PVK in chloroform solvent with a concentration of 5 mg/ml. It has been found that dissolved PVK in chloroform solvent exhibits a high current density.⁴⁶ The hole-conducting polymer PEDOT:PSS was spin coated with a spin speed of 2000 rpm for 60 s. Finally,

silver paste was applied as the top electrode on the prepared device structure.

Characterizations and Measurements

FESEM images were taken using a Hitachi, Japan SU Series at an accelerating voltage of 5 kV. Surface topography and roughness were examined using an atomic force microscope (AFM) Dimension ICON, BRUKER. The UV–visible spectra of the composites were recorded using a UV2450 Shimadzu UV–visible spectrophotometer in the range 350–800 nm. X-ray diffraction (XRD) was recorded using a PANalytical with a nickel filtered X'Pert Pro X-ray diffractometer with monochromatized Cu-K α radiation ($\lambda = 1.541 \text{ \AA}$) in the 2θ range of 10–100°. X-ray photoelectron spectroscopy (XPS) was recorded using a Thermo Scientific NEXSA with monochromatic Al-K α radiation. All samples were analyzed using a micro-focused, monochromated Al K α X-ray source (spot size: 30–400 nm, $h\nu = 1486.6 \text{ eV}$). The K α charge compensation system was employed using low-energy argon ions to prevent any localized charge spread. Fourier transform infrared spectroscopy (FTIR) spectra were recorded using a Shimadzu 8400 spectrometer in the range of 4000–400 cm^{-1} . Raman spectra were recorded using a Horiba LabRAM HR Evolution spectrometer in the backscattering geometry with a 325-nm argon-ion laser as the excitation source. Electrical measurements were tested under a Sci-Tech solar simulator of the light intensity at AM 1.5G (100 mW cm^{-2}). The active device area was 1 cm^2 .

Results and Discussion

Morphological and Optical Characteristics

Figure 2a and b shows typical FESEM images of ZnO nanorods and ZnO-TiO₂ nanosheets grown on ITO-coated flexible PET substrate. The FESEM images reveal the formation of ZnO nanorods spread uniformly all over the surface of the flexible PET substrate. The average diameter of ZnO nanorods is $\sim 150 \text{ nm}$ with side length $\sim 1 \mu\text{m}$ as shown in Fig. 2c. After the addition of TiO₂, the nanostructures observed in higher-magnification FESEM images reveal that the structure of nanosheets is slightly curved, highly dense and represents uneven surface morphology of the 2D network on a larger scale.⁴⁷ The average thickness of ZnO-TiO₂ nanosheets is found to be $\sim 80 \text{ nm}$ as shown in Figure S1 (see supplementary Figure S1), and the average diameter is found to be $\sim 230 \text{ nm}$ as shown in Fig. 2d. After the addition of TiO₂ nanoparticles on the surface of ZnO nanorods using layer-by-layer adsorption and reaction, it can be observed that the mechanism of nucleation growth and kinetics of

morphology evolution from ZnO nanorods to ZnO-TiO₂ nanosheets comprises effects of different parameters such as nature and concentration of precursor and reacting solutions, substrate, growth temperature, growth duration and reaction time. The overall morphology of nanorods showed a dramatic change into nanosheets due to the accumulation of several nanoparticles stacking upon each other in all directions with a high aspect ratio.⁴⁸ It is mentioned that even though the nanoparticles are densely packed randomly, there are still pores among the accumulated nanoparticles which determines the porosity in the nanosheet morphology. The average density of ZnO nanorods and ZnO-TiO₂ nanosheets have been calculated to be $\sim 2.44 \times 10^8/\text{cm}^2$ and $\sim 5 \times 10^8/\text{cm}^2$ as shown in Fig. 2a and b, respectively. The average density of ZnO-TiO₂ nanosheets is higher than that of ZnO nanorods; therefore, the porosity of ZnO-TiO₂ nanosheets is lower than that of ZnO nanorods. The reason for the change in nanosheet diameter may be attributed to the fact that after the addition of TiO₂ nanoparticles, heterogeneous nucleation sites are induced along the lateral direction from the faces of hexagonal ZnO nanorods which leads to growth of highly dense ZnO-TiO₂ nanosheets in random directions.

Energy dispersive X-ray (EDX) analysis was carried out to confirm the chemical composition of TiO₂/ZnO nanostructures. Figure 2e shows EDX analysis of the ZnO-TiO₂ nanosheets. The EDX spectrum confirms the presence of zinc (Zn), titanium (Ti) and oxygen (O). The atomic and weight percentages of Zn, O and Ti are depicted in the inset of Fig. 2e. Figure 3a, b and c represents the AFM micrographs of ZnO nanorods, TiO₂ nanostructures and ZnO-TiO₂ nanosheets obtained in tapping mode. It can be observed that the surface morphology of ZnO-TiO₂ presents a high-density ordered network of nanosheet structure. The average surface roughness of ZnO nanorods, TiO₂ nanostructures and ZnO-TiO₂ nanosheets is measured as 40 nm, 38.2 nm and 96 nm, respectively. The value of average RMS roughness tends to increase with the attachment of TiO₂. This may be attributed to the heterogeneity of the structure formed due to agglomeration after the attachment of TiO₂ nanoparticles. As-deposited TiO₂ thin films are highly resistive due to the presence of defect states may require a light activation mechanism. However, the rougher surfaces responsible for the increase in the interfacial area may result in larger photocurrents.⁴⁹

Figure 4a shows the normalized UV–visible absorption spectra of PVK film, ZnO nanostructures, TiO₂ nanostructures and ZnO-TiO₂ nanosheets. The optical band gap (E_g) of prepared samples has been calculated using Tauc's formula

$$(\alpha h\nu)^2 = A(h\nu - E_g)$$

where α is the absorption coefficient, $h\nu$ is the incident photon energy and A is a constant. Figure 4b represents

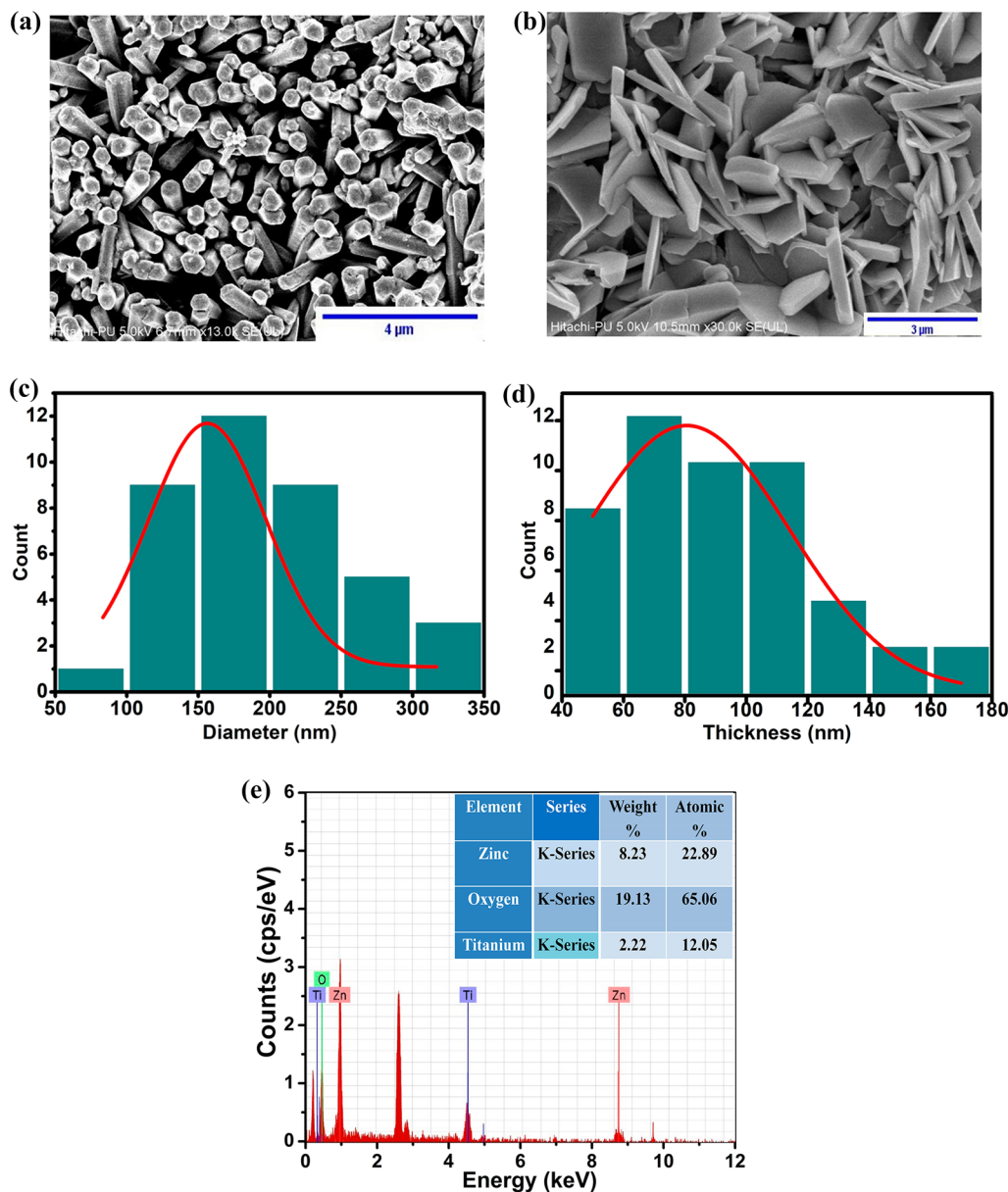


Fig. 2 FESEM micrographs of (a) ZnO nanorods and (b) ZnO-TiO₂ nanosheets. Size distribution histogram showing (c) diameter of ZnO nanorods and (d) diameter of ZnO-TiO₂ nanosheets, (e) EDX analy-

sis of the ZnO-TiO₂ nanosheets; the atomic and weight percentages of Zn, O and Ti are depicted in the inset.

$(\alpha h\nu)^2$ versus $h\nu$ plot for all four samples. The optical band gaps of PVK film, ZnO nanorods, TiO₂ nanostructures and ZnO-TiO₂ nanosheets have been calculated by extrapolation at the linear region of $(\alpha h\nu)^2$ versus $h\nu$ plot to the energy axis. The pristine PVK polymer exhibits two main peaks at 296 nm and 330 nm. The peak at 330 nm is mainly ascribed to $\Pi \rightarrow \Pi^*$ absorption of the carbazole group.^{50,51} The band gap for PVK is calculated as 3.49 eV.^{52,53} The pristine ZnO nanorods show strong absorption in the UV region of wavelength threshold at 315 nm, corresponding

to the energy band gap of 3.67 eV.^{54,55} Also, the pristine TiO₂ shows strong absorption in the UV region of wavelength threshold at 309 nm, corresponding to the energy band gap of 3.52 eV.^{56,57} Because of the formation of nanostructures, the higher band gap values of pristine ZnO and TiO₂ were observed in comparison to that of bulk band gap values, i.e., ~ 3.3 for ZnO and ~ 3.2 for TiO₂. Interestingly, the absorption edge for ZnO-TiO₂ nanosheets has been observed at 315 nm and corresponds to a band gap value of 3.60 eV. The decreased band gap energy of prepared ZnO-TiO₂ nanocomposites compared to pristine ZnO

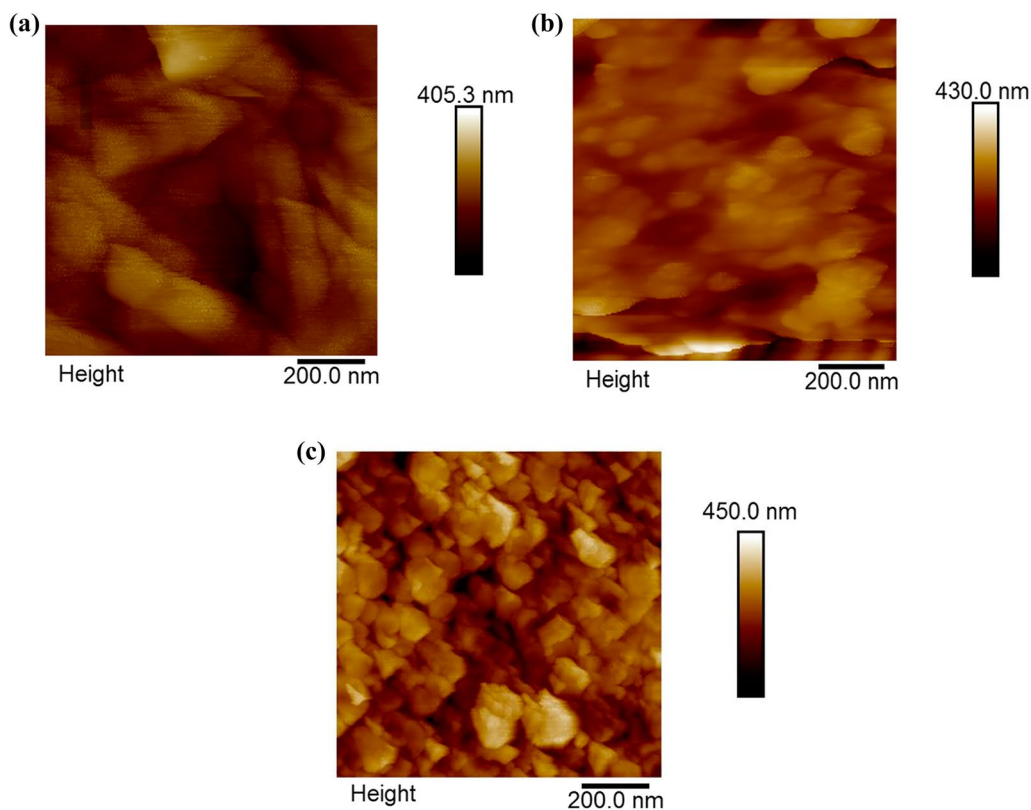


Fig. 3 AFM micrographs of (a) ZnO nanorods, (b) TiO₂ films, and (c) TiO₂/ZnO nanosheets.

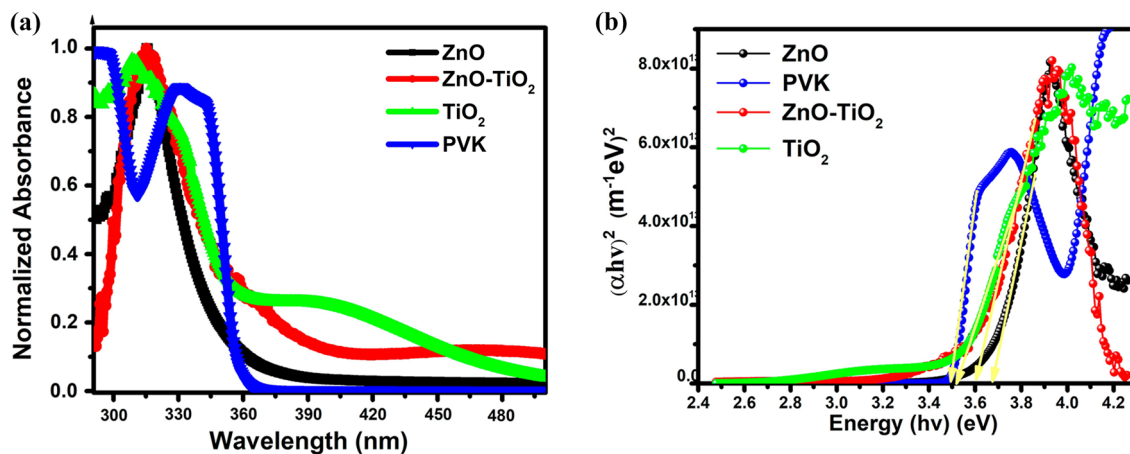


Fig. 4 (a) Normalized UV-Vis absorbance spectra of PVK film, ZnO nanorods, TiO₂ films, ZnO-TiO₂ nanosheets, and (b) Tauc's Plot for the determination of the band gap of prepared samples.

may be due to the coupling effect between ZnO and TiO₂ nanocomposites. Kannan et al. also reported the decreased band gap energy of ZnO nanorods decorated with TiO₂ nanoparticles compared to pristine ZnO nanorod arrays.⁵⁸ This decrease might be because some defect levels are introduced in the forbidden band of ZnO due to formation of additional states lowering the Fermi level which ultimately

result in the decrease of energy band gap. Moreover, the redshift of the optical absorption edge is related to the band gap narrowing accompanied by the merging of the donor and conduction bands.^{58–60} Figure 5 shows the XRD pattern of ZnO nanorods (NRs), TiO₂ nanostructures and TiO₂-decorated ZnO NRs on ITO-coated flexible PET substrate. The XRD pattern of ZnO nanorods, which matches with the

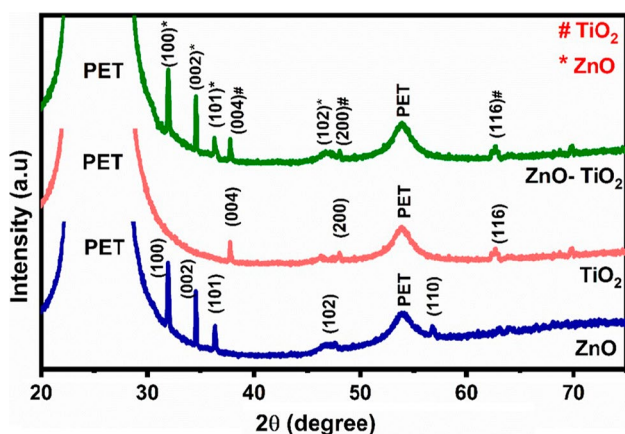


Fig. 5 XRD analysis of TiO₂-ZnO nanosheets, TiO₂ films, and ZnO nanorods on ITO-coated flexible PET substrate.

standard JCPDS Card No. (89-1397), confirms the hexagonal wurtzite structure of ZnO, and the lattice parameters of ZnO nanorods are found to be $a = b = 3.24 \text{ \AA}$ and $c = 5.20 \text{ \AA}$ which is in accordance with the reported literature.^{58,61,62} The sharp diffraction peaks of ZnO nanorods located at $2\theta = 31.7^\circ, 34.36^\circ, 36.02^\circ, 47.47^\circ, 56.4^\circ$ correspond to (100), (002), (101), (102) and (110) planes.⁵⁸ The diffraction peaks in XRD confirm the formation of anatase TiO₂ with a tetragonal crystal structure (JCPDS No. 89-4921), and the values of the lattice parameters of TiO₂ are found to be $a = b = 3.8102 \text{ \AA}$ and $c = 9.6340 \text{ \AA}$ which is in good agreement with the reported value.^{58,62} The sharp diffraction peaks of TiO₂ films located at $2\theta = 38^\circ, 48^\circ, 62.67^\circ, 68.67^\circ$ correspond to (004), (200), (213) and (116) planes.⁶² The anatase form exhibits enhanced photoabsorption in the UV region due to the low recombination rate of charge carriers which is consistent with UV spectroscopy results. The TiO₂-decorated ZnO nanorods show a mixture of ZnO and TiO₂ peaks.^{63,64} The broad and intense diffraction peaks for ZnO NRs show the highly crystalline nature of the prepared films. The two broad diffraction peaks can be observed at 26° and 52.9° due to the diffraction from PET substrate.

Figure 6a shows the X-ray photoelectron spectroscopy (XPS) wide spectra survey of ZnO-TiO₂ nanosheets. In order to correlate the formation of ZnO-TiO₂ nanosheets, XPS study was conducted. The XPS wide spectra survey reveals the presence of Zn, Ti, O and C in the prepared sample. The surface composition was determined by analysis of Zn 2p, Ti 2p, O 1s and C 1s peaks in the XPS spectra as represented in Fig. 6b, c, d, and e.

The Zn 2p and core level observed in the spectra shows a doublet as two deconvoluted peaks located at binding energies 1022.77 eV and 1045.85 eV, allocated to 2p_{3/2} and 2p_{1/2} spin-orbit coupling. It is found that the energy spacing between the two peaks is 23.08 eV and these positions

correspond to typical oxidation state of Zn, i.e. Zn²⁺. This oxidation state corresponds to oxygen-deficient ZnO. The peak positions for Ti 2p_{3/2} and Ti 2p_{1/2} observed, respectively, at 459.18 eV and 464.87 eV are characteristics of Ti-O binding energies in TiO₂ nanoparticles. These binding energy peaks are characteristics of the oxidation state of Ti⁴⁺ octahedral defects in ZnO-TiO₂ nanosheets. O 1s is recorded and fitted in two curves centred at 530.68 eV and 532.37 eV for lattice oxygen and chemisorbed oxygen species, respectively. The low binding energy is from lattice oxygen (O²⁻) in TiO₂ with Ti⁴⁺ ions in the bulk, and the higher binding energy peak is loosely adsorbed oxygen on the surface of TiO₂. The O 1s peak is typical for the presence of oxygen atoms bonded to Zn²⁺ or Ti⁴⁺ in ZnO nanorods and TiO₂ nanoparticles. This binding energy peak is characteristic of the presence of oxygen atoms in metal oxides. The carbon peak (C 1s) binding energy at 285.07 eV is probably a result of exposure of samples to atmospheric hydrocarbons before XPS measurement. The binding energy peak for the C-C/C-H peak for nanostructures is slightly shifted from 286.7 eV to 289.2 eV with energy spacing equivalent to 2.5 eV which confirm the present of TiO₂ on ZnO.⁶⁵⁻⁶⁷

Figure 7a represents the FTIR spectra of ZnO-TiO₂ nanocomposites. The absorption band observed around 517 cm⁻¹ is due to stretching modes of Zn-O. The absorption band around 695 cm⁻¹ is ascribed to vibration modes of Ti-O and Ti-O-C in the nanocomposites.⁶⁸⁻⁷⁰ The broad band noted around 3035 cm⁻¹ corresponds to -OH stretching bonds which is attributed to the presence of moisture in the sample. The low-frequency bands around 1420 and 1557 cm⁻¹ are assigned to C-C stretching bonds. These peaks might be due to the asymmetric and symmetric stretching vibrations of the carboxylic group originating from the reaction intermediates.⁷¹ However, the weak infrared peaks in the region 2315 cm⁻¹-2500 cm⁻¹ might be due to the CO₂ vibration bond absorbed during the annealing process.⁷²

The intense Raman peaks located at frequencies of 225, 333, 406 and 518 cm⁻¹ have been observed for ZnO-TiO₂ nanosheets as depicted in Fig. 7b. The peak located at 225 cm⁻¹ has been assigned to the crystalline structure of wurtzite ZnO. The band around 333 cm⁻¹ is attributed to second-order Raman processes with E₂-E₁ vibration mode of ZnO nanorods. The peaks observed around 406 and 518 cm⁻¹ can be assigned to characteristic Raman active modes of the anatase phase of TiO₂ with symmetries of B_{1g(1)}, A_{1g} + B_{1g(2)}. These peaks have a redshift as compared to standard peaks of anatase TiO₂ located at 395 and 516 cm⁻¹.^{73,74}

Electrical Characteristics

For the investigation of electrical characteristics, the following samples have been prepared as PET/ITO/ZnO-TiO₂/

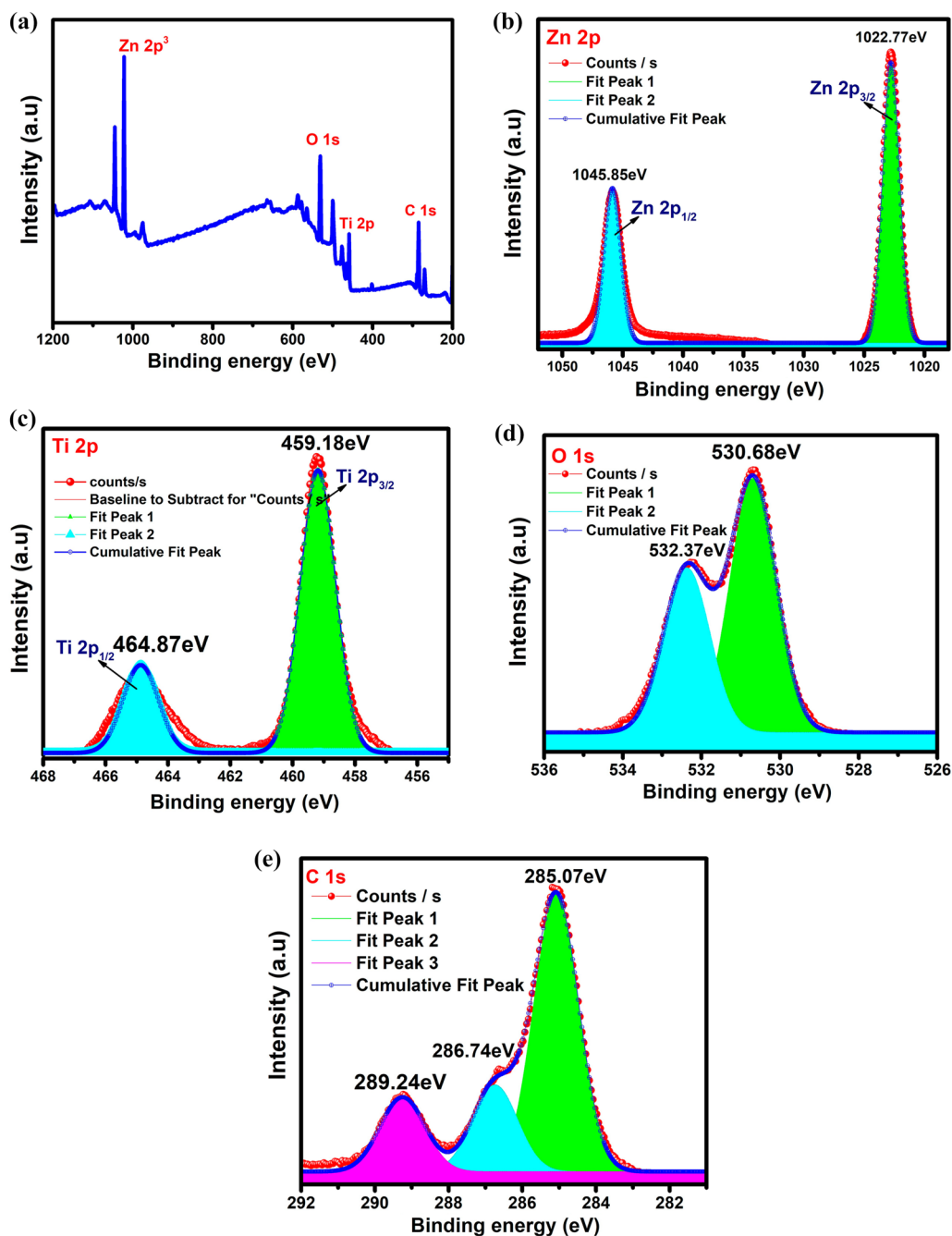


Fig. 6 (a) Represents typical XPS survey scan of ZnO-TiO₂ nanosheets and (b), (c), (d), and (e) represent the high-resolution XPS spectra revealing the chemical states of Zn, Ti, O and C present in the prepared sample, respectively.

PVK/PEDOT:PSS/Ag (denoted as D1), PET/ITO/ZnO/PVK/PEDOT:PSS/Ag (denoted as D2) and PET/ITO/PVK/PEDOT:PSS/Ag (denoted as D3). Figure 8a shows the schematic diagram for of a flexible hybrid photovoltaic D1 device. Figure 8b represents the simplified energy band structure of the hybrid flexible PET/ITO/ZnO-TiO₂/PVK/PEDOT:PSS/Ag photovoltaic device D1 illustrating the working mechanism of the device structure. Energies

are represented in terms of electron Volts (eV) and vacuum energy level as reference. The valence band edges for ZnO, TiO₂, PVK and PEDOT:PSS are 7.4 eV, 7.35 eV, 5.8 eV and 5.2 eV, respectively. The conduction band edges for ZnO, TiO₂, PVK and PEDOT:PSS are 4.2 eV, 4.15 eV, 2.3 eV and 2.2 eV, respectively. The work function for electrodes Ag and ITO are 4.26 eV and 4.2 eV. The values have been reported from the previously reported literature.^{75–80} When

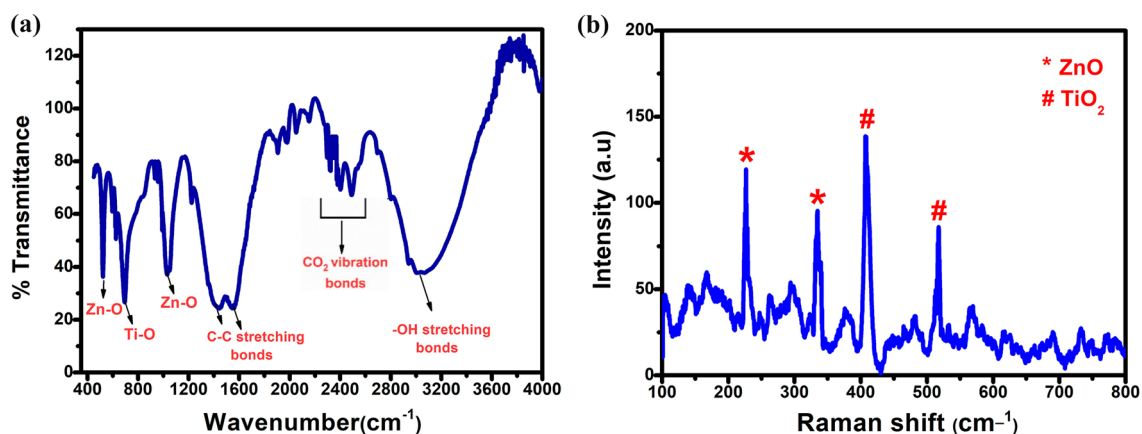


Fig. 7 (a) FTIR spectrum of ZnO-TiO₂ nanosheets and (b) Raman spectrum of ZnO-TiO₂ nanosheets.

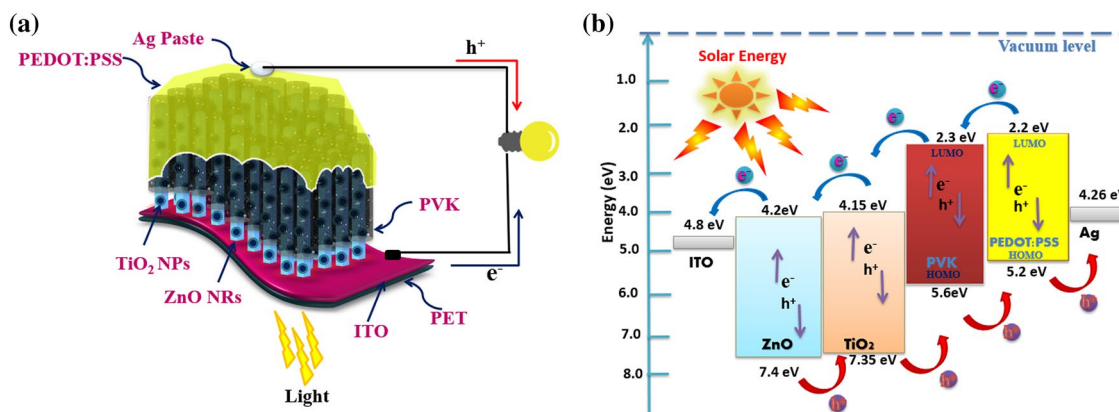


Fig. 8 (a) Schematic diagram of the hybrid D1 device. (b) Illustration of the working mechanism of the D1 device through the energy band diagram.

the light shines on the device, the polymer gets excited. This results in photogeneration of excitons (electron-hole pairs) in polymer PVK and charge separation takes place at the donor-acceptor interface due to the effect of built-in electric field in the space charge region. The electrons are injected from the LUMO of PVK into the conduction band of TiO₂. Meanwhile, the holes can transport from TiO₂ to PVK and from PVK to PEDOT:PSS as the HOMO level of PVK is lower than the HOMO level of PEDOT:PSS and the valence band of TiO₂ is lower than that of PVK. This also minimizes back electron transfer through the barrier imposed by PVK. The charge carriers are collected by respective electrodes which results in the flow of photocurrent in the circuit. This type of cascading band configuration improves the charge transport and reduces the charge recombination by lowering the charge carrier lifetime at the interface.^{81,82} Theoretically the difference between the highest occupied molecular orbital (HOMO) level of the donor and the lowest unoccupied molecular orbital (LUMO) of the acceptor is generally

related to the open-circuit voltage, V_{oc} , of the photovoltaic device, i.e. 1.15 eV.⁸³

In Fig. 9a, the current density versus voltage (J-V) curves for the flexible D1 device tested in the dark and under illumination with the irradiation of a stimulated sunlight (AM 1.5G, 100 mW cm⁻²) are presented. In the dark, the device shows almost negligible reverse bias current. In reverse bias, high energy is required to transport electrons from the anode to the cathode. The negligible amount of current might be due to low shunt resistance values and low density of defects in the photoactive layer. Under illumination, the D1 device shows a short-circuit current density value of 14.94 mA cm⁻² at 0.43 V. This increase in photocurrent value is due to the flow of electrons toward the cathode and the flow of holes towards the anode under the illumination of solar light.

During the electrical measurements, the power conversion efficiency (PCE) and fill factor (FF) of the photovoltaic device have been calculated by using^{84,85}

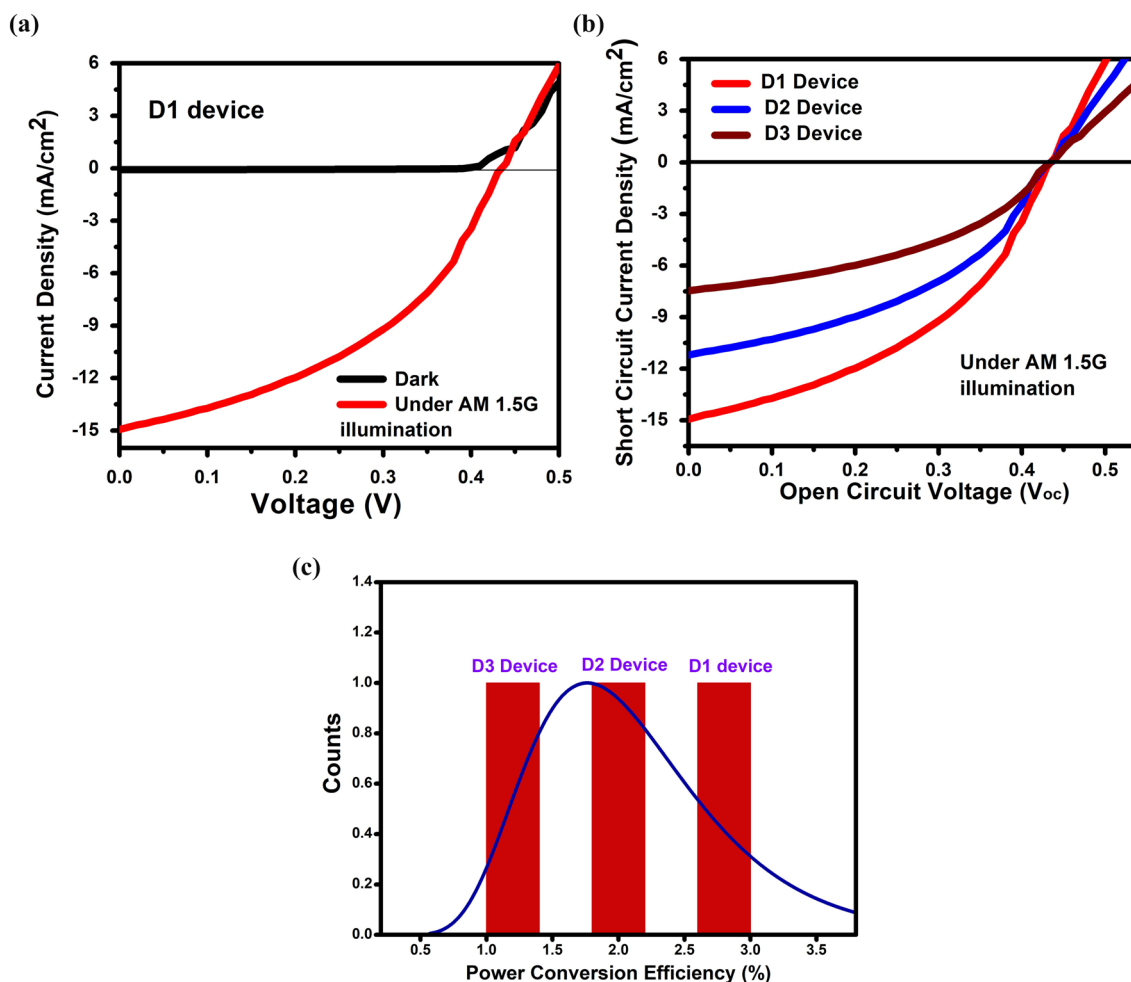


Fig. 9 (a) J-V characteristics of the flexible D1 device under dark and illumination of white light at AM 1.5 intensity irradiance. (b) J-V characteristics of D1, D2 and D3 devices under illumination of white

light at AM 1.5 intensity irradiance. (c) Counts versus PCE (%) histogram distribution for D1, D2 and D3 devices.

$$\eta = \frac{V_{oc} J_{sc} FF}{P_{in}}$$

$$FF = \frac{V_{mp} J_{mp}}{V_{oc} J_{sc}}$$

where P_{in} is the power of incident solar light, η is power conversion efficiency (PCE), FF is the fill factor, V_{mp} is the value of maximum voltage, J_{mp} is the value of maximum current density, V_{oc} and J_{sc} are the open-circuit voltage and short-circuit photocurrent, respectively. In Fig. 9b, the J-V characteristics of D1, D2 and D3 devices are plotted. D2 and D3 exhibit J_{sc} values of 11.20 mA/cm² and 7.47 mA/cm², respectively, at 0.43 V (V_{oc}). The PCE values for D2 and D3 are 2.07% and 1.38%, respectively, and FF for both D2 and D3 is 0.43. For device D3, the PCE value is minimal. In general terms, the organic bilayer solar cells are limited

by low chances of exciton dissociation at the donor-acceptor complex due to larger diffusion length in organic layers and greater possibility of charge recombination.⁸⁶ Charge recombination is still a problem when ZnO alone is added to the electron transporting layer TiO₂. Because of the coupling between ZnO and TiO₂, the recombination rate of the charge carriers is suppressed. If we neglect this coupling, it is seen that the photogenerated electrons and holes quickly recombine in ZnO. But in the case of a heterojunction between ZnO and TiO₂, the photogenerated holes of ZnO easily transfer into the valence band of TiO₂ and electrons of TiO₂ transfer into the conduction band of ZnO which promotes charge separation. Thereby, the main device D1 has been prepared to investigate the role of TiO₂ as the electron transporting layer between an organic donor and inorganic acceptor complex. It has been noted that the short-circuit photocurrent value increases up to 14.94 mA cm⁻² and the

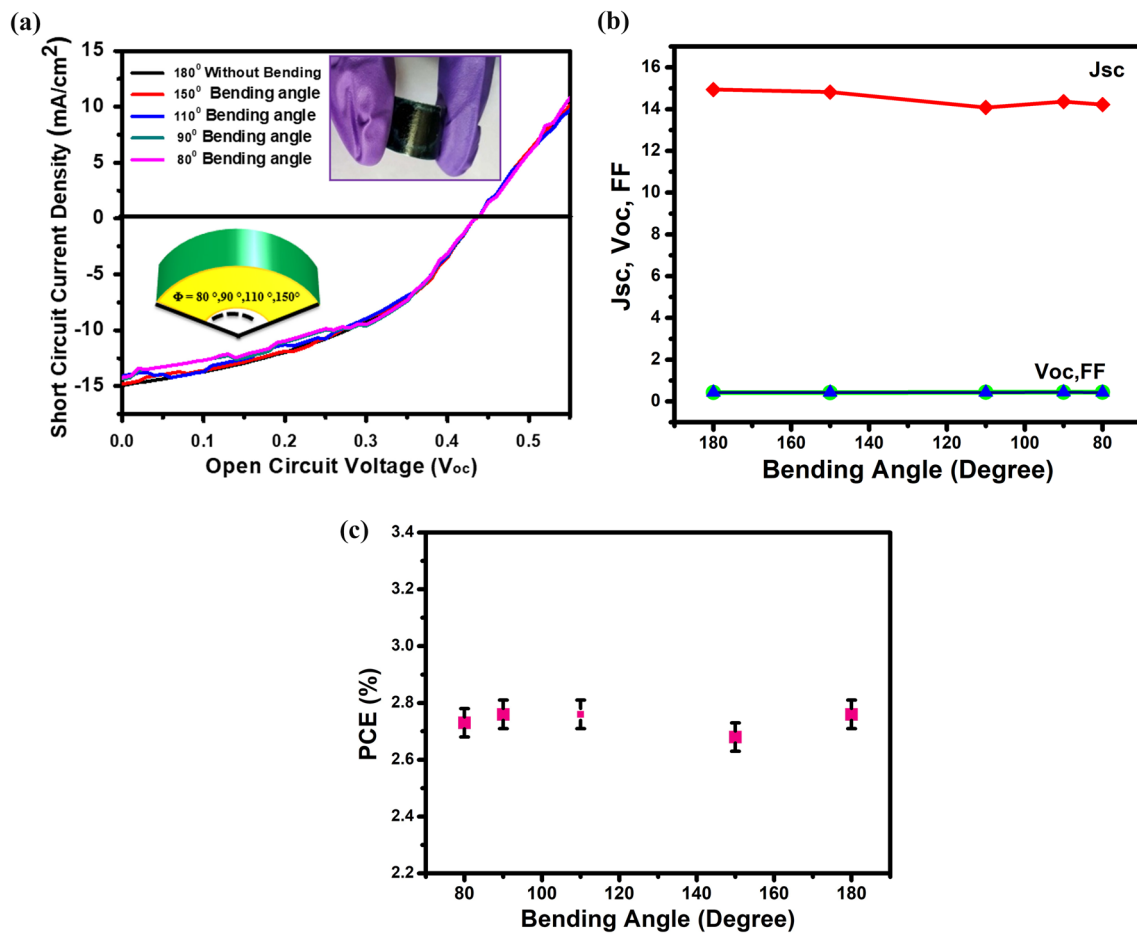


Fig. 10 (a) J-V characteristics of the flexible D1 device for 180° (without bending) and at different bending angles: 80°, 90°, 110° and 150°. Photograph of the flexible D1 device in the inset. (b) Plot of J_{sc} , V_{oc} , FF versus 180° (without bending) and with different bend-

ing angles: 80°, 90°, 110°, 150° of the flexible D1 device. (c) PCE (%) versus 180° (without bending) and with different bending angles: 80°, 90°, 110°, 150° of the flexible D1 device.

Table 1 Solar cell parameters for prepared devices D1, D2 and D3 tested under the irradiation of simulated sunlight (AM 1.5 G, 100mW/cm²)

Device configuration	V_{oc} (V)	J_{sc} (mA/cm ²)	Fill factor (%)	PCE (%)
D1 Device (Ag/PEDOT:PSS/PVK/TiO ₂ -ZnO/ITO/PET)	0.43	14.94	43	2.76
D2 Device (Ag/PEDOT:PSS/PVK/ZnO/ITO/PET)	0.43	11.20	43	2.07
D3 Device (Ag/PEDOT:PSS/PVK/ITO/PET)	0.43	7.47	43	1.38

V_{oc} value remains unchanged at 0.43 V. The PCE of the D1 device also showed an increase in value up to 2.76%.^{87–89}

Figure 9c displays the histogram representing counts versus average PCE (%) of the D1, D2 and D3 devices on flexible substrates. It is clear from the results that TiO₂/ZnO nanosheet-based devices (D1) exhibited high J_{sc} and PCE as compared to ZnO alone (D2) and only organic layer-based devices (D3). The low performance of D2 and D3 may be due to recombination losses as well as pinholes present in the photoactive layer in prepared devices. However, the

optimized performance of the photovoltaic D1 device may be ascribed to the shorter diffusion length, surface passivation and enhanced charge transport ability of TiO₂. The TiO₂/ZnO nanosheets provide increased surface area as well as infiltration of PVK over the nanosheets. This is favourable for enhanced light harvesting which validates the improved performance of the flexible D1 device. Moreover, TiO₂/ZnO co-blocking layer provides dense network of percolation pathways for the transport of charge carriers from the point of injection to the collection at respective electrodes.^{90,91}

Table I elucidates the solar cell parameters determined for the prepared devices D1, D2 and D3 tested under the irradiation of simulated sunlight (AM 1.5 G, 100 mW/cm²). The flexible D1 device shows better PCE compared to D2 and D3 devices due to the presence of an electron transport layer of TiO₂ and hole transport conducting polymer layer of PVK, generating electron–hole pairs at the interface of the TiO₂/PVK heterostructure. The better performance of the D1 device can be possibly credited to the increased interfacial area provided by ZnO–TiO₂ nanosheets, charge injection capability of the TiO₂ layer and improved design of inverted device structure.

Flexible Study of Fabricated Devices

The current–voltage characteristics of flexible D1 device for 180° (without bending) and at different bending angles, 80°, 90°, 110° and 150°, as shown in Fig. 10a. A photograph of the flexible D1 device is shown in the inset. The short-circuit photocurrent (J_{sc}) values for the D1 device are noted as 14.22 mA/cm², 14.36 mA/cm², 14.08 mA/cm², 14.82 mA/cm² and 14.94 mA/cm² after bending at 80°, 90°, 110°, 150° and 180° (without bending), respectively. The open-circuit voltage (V_{oc}) equals 0.43 V which is the same for all bending angles and without bending. The performance of the flexible device D1 was further calculated by plotting J_{sc}, V_{oc} and FF as a variation of different bending angles (80°, 90°, 110°, 150°) and 180° (without bending), as represented in Fig. 10b. There was not much change in the values of parameters J_{sc}, V_{oc} and FF. Moreover, the graph of PCE (%) vs. different bending angles (80°, 90°, 110°, 150°) and 180° (without bending) has been plotted in Fig. 10c. Interestingly, the PCE (%) value of the D1 device remained unchanged even after bending the device at 80°, 90°, 110°, 150°, which demonstrates that the fabricated device D1 is suitable for flexible solar cell applications.

Conclusion

In this work, we have designed a typical flexible device (called D1) solar cell structure and investigated the role of TiO₂/ZnO as a co-blocking layer which results in fewer recombination losses and increased power conversion efficiency. The surface morphology and surface topography have been studied using FESEM and AFM. FESEM micrographs show that the prepared TiO₂/ZnO nanosheets had an arrangement that provided a large interfacial area for charge separation as well as a dense network of conducting pathways for charge transportation. The UV-Vis spectroscopy results revealed the band gap narrowing effect in TiO₂/ZnO nanosheets. The XRD results confirmed the crystalline nature of the prepared samples. The XPS study showed the

available oxidation states of zinc (Zn²⁺) and titanium (Ti⁴⁺) in TiO₂/ZnO nanosheets. FTIR and Raman spectroscopy further confirmed the chemical composition of prepared samples and the presence of vibrational states available in TiO₂/ZnO nanosheets. From the electrical measurements, it has been concluded that the flexible device D1 performed at an optimum level with a maximum PCE value up to 2.76% and fill factor of 43%. This may be due to the addition of TiO₂ which efficiently improved electron transport as well as blocked the back diffusion of holes. The surface passivation by the TiO₂ electron transport layer led to fewer recombination losses which enabled the device to function at its optimum level as compared to control samples. The flexibility test did not degrade the device performance parameters for different bending angles. The fabricated device is a potential candidate in the emerging field of flexible solar cell applications.

Supplementary Information The online version contains supplementary material available at <https://doi.org/10.1007/s11664-022-09815-0>.

Acknowledgments This research work was funded by the Defence Research and Development Organisation (DRDO), Sanction No. F.DFTM/08/3700/Sens/M/P-04, dated 05-Oct-2020, Government of India

Data Availability The data that support the findings of this study are available from the corresponding author upon reasonable request.

Conflicts of interest

There is no conflict to declare.

References

1. S. Sharma, K.K. Jain, and A. Sharma, Solar cells: in research and applications—a review. *Mater. Sci. Appl.* 6, 1145 (2015). <https://doi.org/10.4236/msa.2015.612113>.
2. M. Nikolka, K. Broch, J. Armitage, D. Hanifi, P.J. Nowack, D. Venkateshvaran, and H. Sirringhaus, High-mobility, trap-free charge transport in conjugated polymer diodes. *Nat. Commun.* 10, 1–9 (2019). <https://doi.org/10.1038/s41467-019-10188-y>.
3. A.J. Breeze, Z. Schlesinger, S.A. Carter, and P.J. Brock, Charge transport in TiO₂/M E H– P P V polymer photovoltaics. *Phys. Rev. B* 64, 125205 (2001). <https://doi.org/10.1103/PhysRevB.64.125205>.
4. K.M. Coakley, and M.D. McGehee, Photovoltaic cells made from conjugated polymers infiltrated into mesoporous titania. *Appl. Phys. Lett.* 83, 3380–3382 (2003). <https://doi.org/10.1063/1.1616197>.
5. Q. Fan, B. McQuillin, D.D.C. Bradley, S. Whitelegg, and A.B. Seddon, A solid state solar cell using sol–gel processed material and a polymer. *Chem. Phys. Lett.* 347, 325–330 (2001). [https://doi.org/10.1016/S0009-2614\(01\)01003-X](https://doi.org/10.1016/S0009-2614(01)01003-X).
6. T.J. Savenije, J.M. Warman, and A. Goossens, Visible light sensitisation of titanium dioxide using a phenylene vinylene polymer. *Chem. Phys. Lett.* 287, 148–153 (1998). [https://doi.org/10.1016/S0009-2614\(98\)00163-8](https://doi.org/10.1016/S0009-2614(98)00163-8).
7. A.C. Arango, L.R. Johnson, V.N. Bliznyuk, Z. Schlesinger, S.A. Carter, and H.H. Hörhold, Efficient titanium oxide/

- conjugated polymer photovoltaics for solar energy conversion. *Adv. Mater.* 12, 1689–1692 (2000). [https://doi.org/10.1002/1521-4095\(200011\)](https://doi.org/10.1002/1521-4095(200011)).
8. P. Ravirajan, S.A. Haque, J.R. Durrant, D.D. Bradley, and J. Nelson, The effect of polymer optoelectronic properties on the performance of multilayer hybrid polymer/TiO₂ solar cells. *Adv. Funct. Mater.* 15, 609–618 (2005). <https://doi.org/10.1002/adfm.20040165>.
 9. S.S. Li, and C.W. Chen, Polymer–metal-oxide hybrid solar cells. *J. Mater. Chem. A* 1, 10574–10591 (2013). <https://doi.org/10.1039/C3TA11998J>.
 10. N.J. Jeon, J.H. Noh, Y.C. Kim, W.S. Yang, S. Ryu, and S.I. Seok, Solvent engineering for high-performance inorganic–organic hybrid perovskite solar cells. *Nat. Mater.* 13, 897–903 (2014). <https://doi.org/10.1038/nmat4014>.
 11. D. Liu, and T.L. Kelly, Perovskite solar cells with a planar heterojunction structure prepared using room-temperature solution processing techniques. *Nat. Photonics* 8, 133–138 (2014). <https://doi.org/10.1038/nphoton.2013.342>.
 12. W. Ke, G. Fang, Q. Liu, L. Xiong, P. Qin, H. Tao, and Y. Yan, Low-temperature solution-processed tin oxide as an alternative electron transporting layer for efficient perovskite solar cells. *J. Am. Chem. Soc.* 137, 6730–6733 (2015). <https://doi.org/10.1021/jacs.5b01994>.
 13. Q. Jiang, L. Zhang, H. Wang, X. Yang, J. Meng, H. Liu, and J. You, Enhanced electron extraction using SnO₂ for high-efficiency planar-structure HC (NH₂)₂ PBI 3-based perovskite solar cells. *Nat. Energy* 2, 1–7 (2016). <https://doi.org/10.1038/nenergy.2016.177>.
 14. Y. Zhou, X. Li, and H. Lin, To be higher and stronger—metal oxide electron transport materials for perovskite solar cells. *Small* 16, 1902579 (2020). <https://doi.org/10.1002/sml.201902579>.
 15. Y. Slimani, A. Selmi, E. Hannachi, M.A. Almessiere, A. Baykal, and I. Ercan, Impact of ZnO addition on structural, morphological, optical, dielectric and electrical performances of BaTiO₃ ceramics. *J. Mater. Sci. Mater. Electron.* 30, 9520–9530 (2019). <https://doi.org/10.1007/s10854-019-01284-2>.
 16. Y.M. Sun, J.H. Seo, C.J. Takacs, J. Seiffter, and A.J. Heeger, Inverted polymer solar cells integrated with a low-temperature-annealed sol-gel-derived ZnO film as an electron transport layer. *Adv. Mater.* 23, 1679–1683 (2011). <https://doi.org/10.1002/adma.201004301>.
 17. Y.Y. Wang, I. Fedin, H. Zhang, and D.V. Talapin, Direct optical lithography of functional inorganic nanomaterials. *Science* 357, 385–388 (2017). <https://doi.org/10.1126/science.aan2958>.
 18. F.Y. Wang, L.F. Song, H.C. Zhang, Y. Meng, L.Q. Luo, Y. Xi, L. Liu, N. Han, Z.X. Yang, J. Tang, F.K. Shan, and J. Ho, ZnO nanofiber thin-film transistors with low operating voltages. *Adv. Electron. Mater.* 4, 1700336 (2018). <https://doi.org/10.1002/aelm.201700336>.
 19. G. Kartopu, D. Turkay, C. Ozcan, W. Hadibrata, P. Aurang, S. Yerci, H.E. Unalan, V. Barrioz, Y. Qu, L. Bowen, A.K. Gurlek, P. Maiello, R. Turan, and S.J.C. Irvine, Photovoltaic performance of CdS/CdTe junctions on ZnO nanorod arrays. *Sol. Energy Mater. Sol. Cells* 176, 100–108 (2018). <https://doi.org/10.1016/j.solmat.2017.11.036>.
 20. Y.H. Chen, S.Q. Chu, R.Q. Li, Y.B. Qin, Y.N. Xu, X.W. Zhang, J. Wang, M.J. Liu, W.Y. Lai, and W. Huang, Highly efficient inverted organic light-emitting devices adopting solution-processed double electron-injection layers. *Org. Electron.* 66, 1–6 (2019). <https://doi.org/10.1016/j.orgel.2018.12.008>.
 21. J. Huang, Z. Yin, and Q. Zheng, Applications of ZnO in organic and hybrid solar cells. *Energy Environ. Sci.* 4, 3861–3877 (2011). <https://doi.org/10.1039/C1EE01873F>.
 22. J. Tian, E. Uchaker, Q. Zhang, and G. Cao, Hierarchically structured ZnO nanorods–nanosheets for improved quantum-dot-sensitized solar cells. *ACS Appl. Mater. Interface* 6, 4466–4472 (2014). <https://doi.org/10.1021/am500209f>.
 23. S.H. Bae, H. Zhao, Y.T. Hsieh, L. Zuo, N. De Marco, Y.S. Rim, and Y. Yang, Printable solar cells from advanced solution-processible materials. *Chem* 1, 197–219 (2016). <https://doi.org/10.1016/j.chempr.2016.07.010>.
 24. T. Kim, J. Lim, and S. Song, Recent Progress and Challenges of Electron Transport Layers in Organic-Inorganic Perovskite Solar Cells. *Energies* 13, 5572 (2020). <https://doi.org/10.3390/en13215572>.
 25. E. Hannachi, Y. Slimani, A.T. Okasha, G. Yasin, M. Iqbal, M. Shariq, D. Kaya, F.B. Azzouz, and A. Kkicibil, YBCO superconductor added with one-dimensional TiO₂ nanostructures: Frequency dependencies of AC susceptibility FC-ZFC magnetization, and pseudo-gap studies. *J. Alloy Compd.* 883, 160887 (2021). <https://doi.org/10.1016/j.jallcom.2021.160887>.
 26. K. M.O'Malley, H. L. Yip, A. K. Y. Jen, 2014. Metal oxide interlayer's for polymer solar cells. In *Organic Photovoltaics: Materials, Device Physics, and Manufacturing Technologies*, Wiley, pp. 319. <https://doi.org/10.1002/9783527656912.ch10>
 27. K.Y. Wu, and J.B. Cui, Study of ZnO nanoparticles-decorated TiO₂ 001 facets heterostructures and their photocatalytic activity. *Solid State Phenom.* (2019). <https://doi.org/10.4028/www.scientific.net/SSP>.
 28. D. Fredj, F. Pourcin, R. Alkarsifi, V. Kilinc, X. Liu, S. Ben Dkhil, and M. Boujelbene, Fabrication and characterization of hybrid organic-inorganic electron extraction layers for polymer solar cells toward improved processing robustness and air stability. *ACS Appl. Mater. Interface* 10, 17309–17317 (2018). <https://doi.org/10.1021/acsami.7b16297>.
 29. M. Rani, and S.K. Tripathi, A comparative study of nanostructured TiO₂, ZnO and bilayer TiO₂/ZnO dye-sensitized solar cells. *J. Electron. Mater.* 44, 1151–1159 (2015). <https://doi.org/10.1007/s11664-015-3636-5>.
 30. S. Tang, N. Tang, X. Meng, S. Huang, and Y. Hao, Enhanced power efficiency of ZnO based organic/inorganic solar cells by surface modification. *Phys. E Low Dimens. Syst. Nanostruct.* 83, 398–404 (2016). <https://doi.org/10.1016/j.physe.2016.03.031>.
 31. W.J. Beek, M.M. Wienk, M. Kemerink, X. Yang, and R.A. Janssen, Hybrid zinc oxide conjugated polymer bulk heterojunction solar cells. *J. Phys. Chem. B* 109, 9505–9516 (2005). <https://doi.org/10.1021/jp050745x>.
 32. S. Wang, S. Yang, C. Yang, Z. Li, J. Wang, and W. Ge, Poly (N-vinylcarbazole) (PVK) photoconductivity enhancement induced by doping with CdS nanocrystals through chemical hybridization. *J. Phys. Chem. B* 104, 11853–11858 (2000). <https://doi.org/10.1021/jp0005064>.
 33. S.S. Lo, L. Yang, and C.P. Chiu, ZnO/poly (N-vinylcarbazole) coaxial nanocables for white-light emissions. *J. Mater. Chem. C* 3, 686–692 (2015). <https://doi.org/10.1039/C4TC02187H>.
 34. G. Li, and X. Ni, A novel photoconductive ZnO/PVK nanocomposite prepared through photopolymerization induced by semiconductor nanoparticles. *Mater. Lett.* 62, 3066–3069 (2008). <https://doi.org/10.1016/j.matlet.2008.01.106>.
 35. X. Guo, X. Liu, F. Lin, H. Li, Y. Fan, and N. Zhang, Highly conductive transparent organic electrodes with multilayer structures for rigid and flexible optoelectronics. *Sci. Rep.* 5, 9 (2015). <https://doi.org/10.1038/srep10569>.
 36. S.W. Lee, S.H. Cha, K.J. Choi, B.H. Kang, J.S. Lee, S.W. Kim, and S.W. Kang, Low dark-current, high current-gain of PVK/ZnO nanoparticles composite-based UV photodetector by PN-heterojunction control. *Sensors* 16, 74 (2016). <https://doi.org/10.3390/s16010074>.
 37. A.J. Stapleton, S. Yambem, A.H. Johns, C.T. Gibson, C.J. Shearer, A.V. Ellis, J.G. Shapter, and G.G. Ersson, J.S. Quinton, P.L. Burn, Pathway to high throughput, low cost indium-free transparent

- electrodes. *J. Mater. Chem. A* 3, 13892–1389 (2015). <https://doi.org/10.1039/C5TA03248B>.
38. X. Fan, B.G. Xu, N.X. Wang, J.Z. Wang, S.H. Liu, H. Wang, and F. Yan, Highly conductive stretchable all-plastic electrodes using a novel dipping-embedded transfer method for high-performance wearable sensors and semitransparent organic solar cells. *Adv. Electron. Mater.* 3, 1600471 (2017). <https://doi.org/10.1002/aelm.201600471>.
 39. C.Z. Liao, C.H. Mak, M. Zhang, H.L.W. Chan, and F. Yan, Flexible organic electrochemical transistors for highly selective enzyme biosensors and used for saliva testing. *Adv. Mater.* 27, 676–681 (2015). <https://doi.org/10.1002/adma.201404378>.
 40. S. Jäckle, M. Mattiza, M. Liebhaber, G. Brönstrup, M. Rommel, K. Lips, and S. Christiansen, Junction formation and current transport mechanisms in hybrid n-Si/PEDOT: PSS solar cells. *Sci. Rep.* 5, 1–12 (2015). <https://doi.org/10.1038/srep13008>.
 41. C. Thu, P. Ehrenreich, K.K. Wong, E. Zimmermann, J. Dorman, W. Wang, and L. Schmidt-Mende, Role of the metal-oxide work function on photocurrent generation in hybrid solar cells. *Sci. Rep.* 8, 1–8 (2018). <https://doi.org/10.1038/s41598-018-21721-2>.
 42. I. Gonzalez-Valls, and M. Lira-Cantu, Vertically-aligned nanostructures of ZnO for excitonic solar cells: a review. *Energy Environ. Sci.* 2, 19–34 (2009). <https://doi.org/10.1038/s41598-018-21721-2>.
 43. J.J.L. Hmar, T. Majumder, S. Dhar, and S.P. Mondal, Sulfur and nitrogen co-doped graphene quantum dot decorated ZnO nanorod/polymer hybrid flexible device for photosensing applications. *Thin Solid Films* 612, 274–283 (2016). <https://doi.org/10.1016/j.tsf.2016.06.014>.
 44. S.H. Ko, D. Lee, H.W. Kang, K.H. Nam, J.Y. Yeo, S.J. Hong, and H.J. Sung, Nanoforest of hydrothermally grown hierarchical ZnO nanowires for a high efficiency dye-sensitized solar cell. *Nano letters* 11, 666–671 (2011). <https://doi.org/10.1021/nl1037962>.
 45. X. Yin, W. Que, D. Fei, H. Xie, and Z. He, Effect of TiO₂ shell layer prepared by wet-chemical method on the photovoltaic performance of ZnO nanowires arrays-based quantum dot sensitized solar cells. *Electrochim. Acta* 99, 204–210 (2013). <https://doi.org/10.1016/j.electacta.2013.03.110>.
 46. K. Onlaor, N. Chaithanatkun, and B. Tunhoo, Electrical mechanisms of bi-stable memory devices based on an Al/PVK: ZnO NPs/ITO structure with different ZnO NPs annealing temperatures. *Curr. Appl. Phys.* 16, 1418–1423 (2016). <https://doi.org/10.1016/j.orgel.2014.03.024>.
 47. Y.C. Liang, Y.C. Chang, and W.C. Zhao, Design and synthesis of novel 2D porous zinc oxide-nickel oxide composite nanosheets for detecting ethanol vapor. *J. Nanomater.* 10, 1989 (2020). <https://doi.org/10.3390/nano10101989>.
 48. A. Umar, M.S. Akhtar, M.S. Al-Assiri, A. Al-Hajry, H. Algarni, V.R. de Mendonça, Y. Masuda, S.H. Kim, and Q.I. Rahman, Highly porous ZnO nanosheets self-assembled in rosette-like morphologies for dye-sensitized solar cell application. *New J. Chem.* 39, 7961–7970 (2015). <https://doi.org/10.1039/c5nj00551e>.
 49. X. Hu, Z. Huang, X. Zhou, P. Li, Y. Wang, Z. Huang, and Y. Song, Wearable large-scale perovskite solar-power source via nanocellular scaffold. *Adv. Mater.* 29, 1703236 (2017). <https://doi.org/10.1002/adma.201703236>.
 50. P.X. Thinh, C. Basavaraja, D.G. Kim, and D.S. Huh, Characterization and electrochemical behaviors of honeycomb-patterned poly (N-vinylcarbazole)/polystyrene composite films. *Polym. Bull.* 69, 81–94 (2012). <https://doi.org/10.1007/s00289-012-0727-9>.
 51. M.Y. Oide, K.R. Onmori, I.F. Oppenheim, and S.H. Wang, White electroluminescence from aluminum zinc oxide embedded in poly (9-vinylcarbazole). *Chemistry Select* 4, 12424–12427 (2019). <https://doi.org/10.1002/slct.201902559>.
 52. S. Azizi, M. Belhaj, S. Zargouni, and C. Dridi, Correlation between composition, morphology and optical properties of PVK:n-ZnO:CTAB thin films. *Appl. Phys. A* 123, 475 (2017). <https://doi.org/10.1007/s00339-017-1095-y>.
 53. T.M. Fulghum, P. Taranekar, and R.C. Advincula, Grafting hole-transport precursor polymer brushes on ITO electrodes: surface-initiated polymerization and conjugated polymer network formation of PVK. *Macromolecules* 41, 5681–5687 (2008). <https://doi.org/10.1021/ma800341a>.
 54. M.K. Debanath, and S. Karmakar, Study of blueshift of optical band gap in zinc oxide (ZnO) nanoparticles prepared by low-temperature wet chemical method. *Mater. Lett.* 111, 116–119 (2013). <https://doi.org/10.1016/j.matlet.2013.08.069>.
 55. S.W. Balogun, Y.K. Sanusi, and A.O. Aina, Impact of post-deposition heat treatment on the morphology and optical properties of zinc oxide (ZnO) thin film prepared by spin-coating technique. *J. Photon. Mater. Technol.* 3, 20–28 (2017). <https://doi.org/10.11648/j.jmpt.20170303.11>.
 56. S. Valencia, J.M. Marín, and G. Restrepo, Study of the bandgap of synthesized titanium dioxide nanoparticles using the Sol-Gel method and a hydrothermal treatment. *Open Mater. Sci. J.* 4, 9–14 (2010). <https://doi.org/10.2174/1874088X01004010009>.
 57. C.A. D'Amato, R. Giovannetti, M. Zannotti, E. Rommozzi, M. Minicucci, R. Gunnella, and A.D. Cicco, Band gap implications on Nano-TiO₂ surface modification with ascorbic acid for visible light-active polypropylene coated photocatalyst. *Nanomaterials* 5, 599 (2018). <https://doi.org/10.3390/nano8080599>.
 58. S. Kannan, N.P. Subiramaniam, and S.U. Lavanisadevi, Dye-sensitized solar cells based on TiO₂ nanoparticles-decorated ZnO nanorod arrays for enhanced photovoltaic performance. *J. Mater. Sci. Mater. Electron.* 31, 8514–8522 (2020). <https://doi.org/10.1007/s10854-020-03387-7>.
 59. J. Chen, W. Liao, Y. Jiang, D. Yu, M. Zou, H. Zhu, and M. Du, Facile fabrication of ZnO/TiO₂ heterogeneous nanofibres and their photocatalytic behaviour and mechanism towards Rhodamine B. *Nanomater. Nanotechnol.* 6, 9 (2016). <https://doi.org/10.5772/62291>.
 60. G. Tang, H. Liu, and W. Zhang, The variation of optical band gap for ZnO: In films prepared by sol-gel technique. *Adv. Mater. Sci. Eng.* (2013). <https://doi.org/10.1155/2013/348601>.
 61. M. Achehboune, M. Khenfouch, I. Boukhoubza, I. Derkaoui, L. Leontie, A.B. Carlescu, B.M. Mothudi, I. Zorkani, and A. Jorio, Optimization of the luminescence and structural properties of Er-doped ZnO nanostructures: effect of dopant concentration and excitation wavelength. *J. Lumin.* 246, 118843 (2022). <https://doi.org/10.1016/j.jlumin.2022.118843>.
 62. D. Upadhaya, P. Kumar, and D.D. Purkayastha, Superhydrophobic ZnO/TiO₂ heterostructure with significantly enhanced photocatalytic activity. *J. Mater. Sci. Mater. Electron.* 30, 10399–10407 (2019). <https://doi.org/10.1007/s10854-019-01381-2>.
 63. V. Mishra, M.K. Warshi, A. Sati, A. Kumar, V. Mishra, R. Kumar, and P.R. Sagdeo, Investigation of temperature-dependent optical properties of TiO₂ using diffuse reflectance spectroscopy. *SN Appl. Sci.* 1, 1–8 (2019). <https://doi.org/10.1007/s42452-019-0253-6>.
 64. J. Moma, J. Baloyi, Modified titanium dioxide for photocatalytic applications. *Photocatalysts-Applications and Attributes*, (2019) pp.18. DOI: <https://doi.org/10.5772/intechopen.79374>
 65. K. Davis, R. Yarbrough, M. Froeschle, J. White, and H. Rathnayake, Band gap engineered zinc oxide nanostructures via a sol-gel synthesis of solvent driven shape-controlled crystal growth. *RSC adv.* 9, 14638–14648 (2019). <https://doi.org/10.1039/C9RA02091H>.
 66. K. Wu, X. Dong, J. Zhu, P. Wu, C. Liu, Y. Wang, and X. Guo, Designing biomimetic porous celery: TiO₂/ZnO nanocomposite for enhanced CO₂ photoreduction. *J. Mater. Sci.* 53, 11595–11606 (2018).
 67. M. Kwiatkowski, I. Bezverkhy, and M. Skompska, ZnO nanorods covered with a TiO₂ layer: simple sol-gel preparation, and optical,

- photocatalytic and photoelectrochemical properties. *J. Mater. Chem A* 3, 12748–12760 (2015). <https://doi.org/10.1039/C5TA01087J>.
68. D. Sethi, and R. Sakthivel, ZnO/TiO₂ composites for photocatalytic inactivation of escherichia coli. *J. Photochem. Photobio. B Bio.* 168, 117–123 (2017). <https://doi.org/10.1016/j.jphotobiol.2017.02.005>.
69. M. Khan, A.H. Naqvi, and M. Ahmad, Comparative study of the cytotoxic and genotoxic potentials of zinc oxide and titanium dioxide nanoparticles. *Toxicol. Rep.* 2, 765–774 (2015). <https://doi.org/10.1016/j.toxrep.2015.02.004>.
70. N. Laid, N. Bouanimba, A. Ben Ahmede, A. Toureche, and T. Sehili, Characterization of ZnO and TiO₂ nanopowders and their application for photocatalytic water treatment. *Acta Phys. Pol. A* (2020). <https://doi.org/10.12693/APhysPolA.137.305>.
71. S.J. Mofokeng, V. Kumar, R.E. Kroon, and O.M. Ntwaeaborwa, Structure and optical properties of Dy³⁺ activated sol-gel ZnO-TiO₂ nanocomposites. *J. Alloy. Compd.* 711, 121–131 (2017). <https://doi.org/10.1016/j.jallcom.2017.03.345>.
72. E. Rusman, H. Heryanto, A.N. Fahri, I. Mutmainna, D. Tahir green synthesis ZnO/TiO₂ for high recyclability rapid sunlight photodegradation textile dyes applications. (2021). <https://doi.org/10.21203/rs.3.rs-414953/v1>
73. L. Lin, Y. Yang, L. Men, X. Wang, D. He, Y. Chai, and Q. Tang, A highly efficient TiO₂@ ZnO n-p-n heterojunction nanorod photocatalyst. *Nanoscale* 5, 588–593 (2013). <https://doi.org/10.1039/C2NR33109H>.
74. L. Gu, K. Zheng, Y. Zhou, J. Li, X. Mo, G.R. Patzke, and G. Chen, Humidity sensors based on ZnO/TiO₂ core/shell nanorod arrays with enhanced sensitivity. *Sens. Actuators B: Chem.* 159, 1–7 (2011). <https://doi.org/10.1016/j.snb.2010.12.024>.
75. O.F. Yilmaz, S. Chaudhary, and M. Ozkan, A hybrid organic-inorganic electrode for enhanced charge injection or collection in organic optoelectronic devices. *Nanotechnology* 17, 3662 (2006). <https://doi.org/10.1088/0957-4484/17/15/007>.
76. J.H. Jung, M.Y. Ha, D.Y. Park, M.J. Lee, S.J. Choi, and D.G. Moon, Effect of hole transporting materials on the emission characteristics of soluble processed organic light-emitting devices on the plastic substrate. *Mol. Cryst. Liq. Cryst.* 644, 214–220 (2017). <https://doi.org/10.1080/15421406.2017>.
77. J. Duan, Y. Liu, X. Chen, S. Huang, W. Ou-Yang, G. Zhu, and Z. Sun, Efficient and stable mesoporous perovskite solar cells using p-type poly (9-vinylcarbazole) modified the interface of perovskite/mesoporous TiO₂ layers. *Org. Electron.* 82, 105737 (2020). <https://doi.org/10.1016/j.orgel.2020.105737>.
78. R. Wang, H. Tan, Z. Zhao, G. Zhang, L. Song, W. Dong, and Z. Sun, Stable ZnO@ TiO₂ core/shell nanorod arrays with exposed high energy facets for self-cleaning coatings with anti-reflective properties. *J. Mater. Chem. A* 2, 7313–7318 (2014).
79. Z. Lin, C. Jiang, C. Zhu, and J. Zhang, Development of inverted organic solar cells with TiO₂ interface layer by using low-temperature atomic layer deposition. *ACS Appl. Mater. Interface* 5, 713–718 (2013). <https://doi.org/10.1021/am302252p>.
80. S.J. Lee, H.P. Kim, and A. R. bin Mohd Yusoff, Jang, J., Organic photovoltaic with PEDOT: PSS and V2O5 mixture as hole transport layer. *Sol. Energy Mater. Sol. Cell* 120, 238–243 (2014). <https://doi.org/10.1016/j.solmat.2013.09.009>.
81. Y. Chen, W. Tang, Y. Wu, R. Yuan, J. Yang, W. Shan, and W.H. Zhang, Multilayer cascade charge transport layer for high-performance Inverted mesoscopic all-inorganic and hybrid wide-band-gap perovskite solar cells. *Sol. RRL* 4, 2000344 (2020). <https://doi.org/10.1002/solr.202000344>.
82. A. Ramar, R. Saraswathi, M. Rajkumar, and S.M. Chen, Influence of poly (n-vinylcarbazole) as a photoanode component in enhancing the performance of a dye-sensitized solar cell. *J. Phys. Chem. C* 119, 23830–23838 (2015). <https://doi.org/10.1021/acs.jpcc.5b06582>.
83. Y. Li, S. Li, L. Jin, J.B. Murowchick, and Z. Peng, Carbon nanoparticles as an interfacial layer between TiO₂-coated ZnO nanorod arrays and conjugated polymers for high-photocurrent hybrid solar cells. *RSC Adv.* 3, 16308–16312 (2013). <https://doi.org/10.5772/67616>.
84. T. Dittrich, Basic characteristics and characterization of solar cells. *Sol. Energy Mater. Sol. Cell* (2018). https://doi.org/10.1142/9781786344496_0001.
85. S.M. Sze, and K.K. Ng, *Physics of semiconductor devices: sze/physics*, 3rd ed., (New York: Wiley, 2014).
86. S. Lattante, Electron and hole transport layers: their use in inverted bulk heterojunction polymer solar cells. *Electronics* 3, 132–164 (2014). <https://doi.org/10.3390/electronics3010132>.
87. Y.Y. Lin, C.W. Chen, T.H. Chu, W.F. Su, C.C. Lin, C.H. Ku, and C.H. Chen, Nanostructured metal oxide/conjugated polymer hybrid solar cells by low temperature solution processes. *J. Mater. Chem.* 17, 4571–4576 (2007). <https://doi.org/10.1039/B710400F>.
88. S. Noor, S. Sajjad, S.A.K. Leghari, S. Shaheen, and A. Iqbal, ZnO/TiO₂ nanocomposite photoanode as an effective UV-vis responsive dye sensitized solar cell. *Mater. Res. Express* 5, 095905 (2018). <https://doi.org/10.1088/2053-1591/aad8ee>.
89. Y. Yang, J. Zhao, C. Cui, Y. Zhang, H. Hu, L. Xu, and W. Tang, Hydrothermal growth of ZnO nanowires scaffolds within mesoporous TiO₂ photoanodes for dye-sensitized solar cells with enhanced efficiency. *Electrochim. Acta* 196, 348–356 (2016). <https://doi.org/10.1016/j.electacta.2016.03.022>.
90. Z. Qiu, C. Liu, G. Pan, W. Meng, W. Yue, J. Chen, and M. Wang, Solution-processed solar cells based on inorganic bulk heterojunctions with evident hole contribution to photocurrent generation. *Phys. Chem. Chem. Phys.* 17, 12328–12339 (2015). <https://doi.org/10.1039/C5CP00030K>.
91. S. Bi, Y. Li, Y. Liu, Z. Ouyang, and C. Jiang, Physical properties of 2D and 3D ZnO materials fabricated by multi-methods and their photoelectric effect on organic solar cells. *J. Sci. Adv. Mater. Device.* 3, 428–432 (2018). <https://doi.org/10.1016/j.jsamd.2018.11.003>.

Publisher's Note Springer Nature remains neutral with regard to jurisdictional claims in published maps and institutional affiliations.